Pure Appl. Geophys. 175 (2018), 3653–3670

https://doi.org/10.1007/s00024-018-1917-7

Pure and Applied Geophysics

Assessment and Adaptive Correction of Observations in Atmospheric Sounding Channels of the Satellite Microwave Radiometer MTVZA-GY

Dmitry Gayfulin,[1] Michael Tsyrulnikov,[1] and Alexander Uspensky[2]

Abstract—The microwave radiometer MTVZA-GY on board the Russian polar orbiting meteorological satellite Meteor-M N2 is briefly described. Errors and biases in antenna brightness temperatures are documented. Observation errors are found to be dependent on the solar angles. An adaptive bias correction technique for MTVZA-GY antenna temperatures is motivated and developed. The technique accounts for the solar angles and sequentially assimilates observed minus simulated radiances in a perpetual 24 h cycle in order to estimate up-to-date correction coefficients defined to be functions of the zenith and azimuth solar angles. The simulated radiances are computed by the RTTOV radiative transfer model from three-dimensional numerical weather prediction fields. The correction technique is implemented for atmospheric temperature and humidity sounding channels of MTVZA-GY. The corrected observations are shown to be significantly more accurate as compared with raw antenna temperatures and with observations that undergo simpler and more traditional corrections. The accuracy of corrected MTVZA-GY observations is compared with the accuracy of AMSU-A and MHS data.

Key words: Satellite observations, microwave radiances, bias correction, data assimilation.

1. Introduction

Observations of the Earth atmosphere made from spacecraft are now a critically important component of the global meteorological observing system. While conventional observations like surface stations, aircraft observations, and radiosondes remain essential in the Northern Hemisphere and, together with radar data, dominate on the regional and local scale, satellite data prevail in the Southern Hemisphere and have a profound impact on the global numerical weather prediction in general (see, e.g., Fig.3 in McNally 2014). Among enormous amounts of meteorologically relevant information acquired by sensors on board multiple geostationary and polar orbiting satellites, the most influential are observations of infrared and microwave radiation leaving the Earth's atmosphere. The outstanding role of radiance observations in the present-day meteorology stems from their sensitivity to atmospheric temperature and humidity profiles at the wide range of altitudes, high horizontal resolution, and global coverage.

The satellite Earth observation system Meteor-3M is being developed in Russia as part of the global observing system. The Meteor-3M system is planned to include new-generation polar-orbiting meteorological satellites of Meteor-M type. In July 2014, one of such satellites, Meteor-M N2, was launched in a sun-synchronous orbit at the altitude of about 832 km. The equator crossing local solar time is 9:30 am and pm for descending and ascending nodes, respectively.[1] The orbital period is approximately 102 min. For more information on Meteor-M N2 as well as on the Meteor-3M ground segment, see Asmus et al. (2014). The payload of Meteor-M N2 includes two atmospheric sounders: the hyper-spectral infrared sounder IKFS-2 and the microwave imager/sounder MTVZA-GY. Data from both sensors are intended for applications in operational meteorology (weather and climate predictions and studies).

In rest of the paper, we outline the MTVZA-GY radiometer, characterize its frequency channels, motivate and present a new solar-angles dependent bias correction technique, and finally show the effect

[1] Hydrometeorological Center of Russia, 11-13, B.Predtechensky Lane, 123242 Moscow, Russia. E-mail: michael.tsyrulnikov@gmail.com

[2] State Research Center "Planeta", 7, B.Predtechensky Lane, 123242 Moscow, Russia.

[1] The descending (ascending) node is the part of the satellite's polar orbit on which it moves southward (northward).

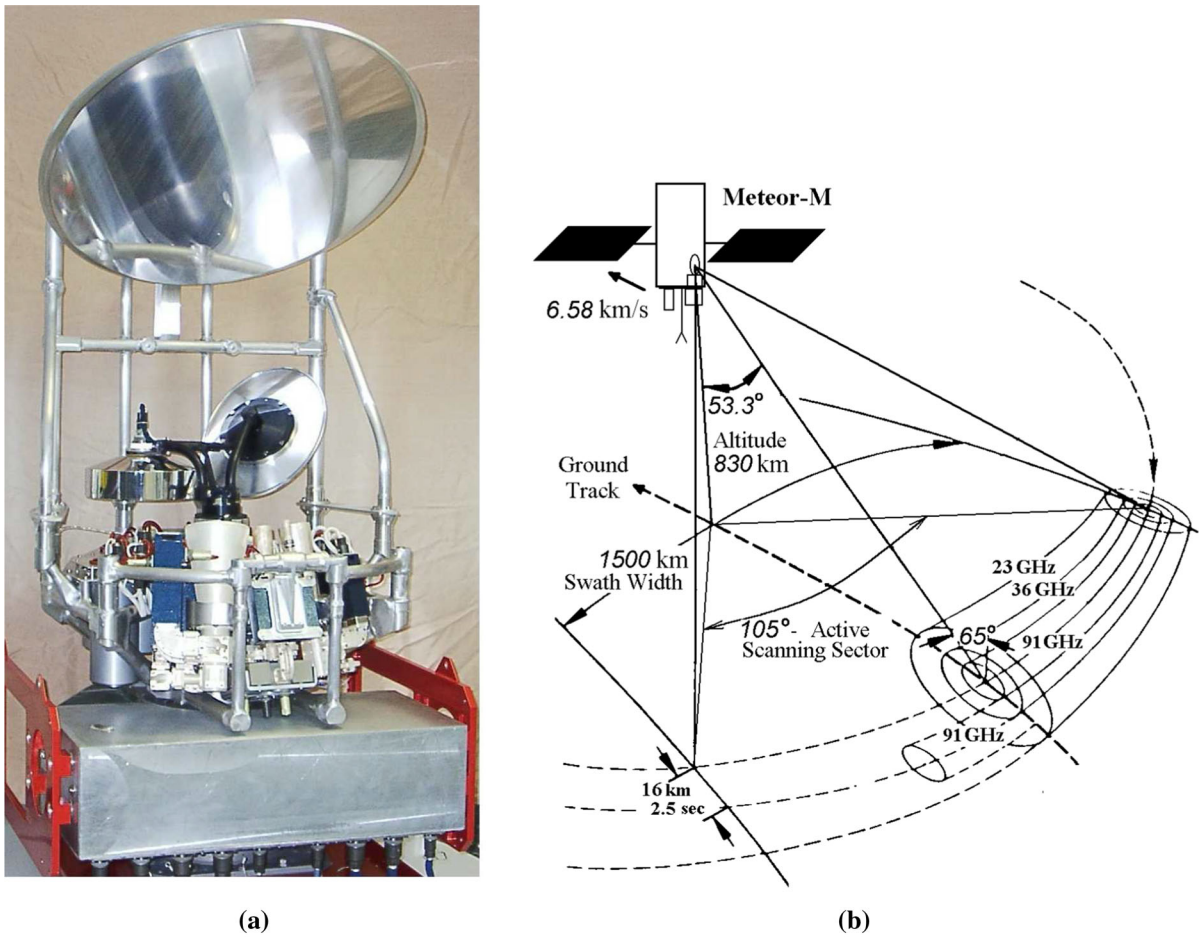

Figure 1
Microwave imager/sounder MTVZA-GY. **a** Photograph showing the main 65-cm antenna reflector at the top, the cold target calibration reflector in the middle, and the drum assembly at the bottom. **b** The scanning geometry

of the correction on the accuracy of the data. We examine channels influenced primarily by atmospheric temperature and humidity (i.e. channels with dominant contributions from surface properties, cloud fields, and precipitation are not considered in this paper).

2. *Brief Description of the MTVZA-GY Radiometer*

MTVZA-GY (where MTVZA is the Russian abbreviation for "module for temperature and humidity sounding of the atmosphere" and "GY" are the initials of the prominent Russian space engineer G.Ya.Guskov) is a 29-channel microwave imaging/sounding radiometer with conical scan geometry. Figure 1 (borrowed with permission from Cherny et al. 2010) shows the radiometer and its scanning geometry. The main characteristics of MTVZA-GY are the following. The viewing angle is 53.3°. The incidence angle with respect to the Earth surface is 65°. The geolocation accuracy is about 40 km.[2] The swath width is 1500 km. The MTVZA-GY scanning platform period is 2.5 s, during which the sub-satellite point travels 16 km.

Table 1 [whose contents are borrowed with permission from Gorobets et al. (2007)] presents more

[2] Is expected to be improved with MTVZA-GY radiometers on the next Meteor-M satellites.

Table 1

MTVZA-GY frequency channel characteristics

N (rttov)	(*N*) (mtvza)	f_c (GHz)	Pol. (V/H)	n_b	Δf (MHz)	FOV (km)	Pixel (km)	σ_T (K)
1,2	1,2	10.65 (window)	V, H	1	100	89 × 198	32 × 32	0.5
3,4	3,4	18.7 (window)	V, H	1	200	52 × 116	32 × 32	0.4
5,6	5,6	23.8 (window)	V, H	1	400	42 × 94	32 × 32	0.3
7,8	26,27	31.5 (window)	V, H	1	1000	35 × 76	32 × 32	0.3
9,10	7,8	36.5 (window)	V, H	1	1000	30 × 67	32 × 32	0.3
11,12	–	42.0 (window)	V, H	1	1000	26 × 60	32 ×32	0.4
13,14	–	48.0 (window)	V, H	1	1000	24 × 43	32 × 32	0.4
15	11	52.80	V	1	400	21 × 48	48 × 48	0.4
16	12	53.30	V	1	400	21 × 48	48 × 48	0.4
17	13	53.80	V	1	400	21 × 48	48 × 48	0.4
18	14	54.64	V	1	400	21 × 48	48 × 48	0.4
19	15	55.63	V	1	400	21 × 48	48 × 48	0.4
20	16	$f0 \pm 0.3222 \pm 0.1$	V	4	50	21 × 48	48 × 48	0.4
21	17	$f0 \pm 0.3222 \pm 0.05$	V	4	20	21 × 48	48 × 48	0.7
22	18	$f0 \pm 0.3222 \pm 0.025$	V	4	10	21 × 48	48 × 48	0.9
23	19	$f0 \pm 0.3222 \pm 0.01$	V	4	5	21× 48	48 × 48	1.3
24	20	$f0 \pm 0.3222 \pm 0.005$	V	4	3	21× 48	48 × 48	1.7
25,*26*	9,*10*	91.65 (window)	V, H	2	2500	14 × 30	16 × 16	0.6
27	21	183.31 ± 7.0	V	2	1500	9 × 21	32 × 32	0.5
28	23	183.31 ± 3.0	V	2	1000	9 × 21	32 × 32	0.6
29	22	183.31 ± 1.4	V	2	500	9 × 21	32 × 32	0.8

Numbers of the available channels are indicated in bold face, whereas the the numbers of the unavailable channels are given in italic

$f_0 = 57.290344$ GHz.

N is the channel number. Channel *26* is not operational and channels *11–14* are missing in raw data files, *rttov* stands for the RTTOV channel numbering (used throughout the paper), *mtvza* is the internal MTVZA-GY channel numbering (not referenced in the paper, given here only for those who intend to use MTVZA-GY data files), f_c is the center frequency of the channel (GHz), *Pol.* is the polarization (V is vertical, H is horizontal), n_b is the number of passbands, Δf the band width (MHz), FOV is the effective field of view (along-scan-line × along-track, km), *Pixel* (along-scan-line × along-track, km) is the 2D moving average window, σ_T is the radiometric noise level (Noise Equivalent ΔT, NEΔT, K), *(window)* marks atmospheric window channels

detailed characteristics of the MTVZA-GY frequency channels, including technical characteristics like frequencies, polarization, and passbands and more meteorologically relevant characteristics like the size of the effective field of view (FOV), the pixel size, and the radiometric noise level.

The FOV characterizes the spot on the surface "seen" by the sensor's antenna; it decreases with the growing frequency (following the wavelength). The pixel is the moving two-dimensional window over which the antenna temperatures are additionally averaged (in order to improve the signal-to-noise ratio). The distance between adjacent MTVZA-GY observations provided to the user is 16 km both in the along-scanline and in the along-track directions.

It is essential for this study that MTVZA-GY is supported by the fast radiative transfer model RTTOV (Saunders et al. 1999) starting from its version 11. Throughout the paper, the RTTOV v.11 channel numbering convention is used, see column 1 of Table 1.

In this work, we examine only *atmospheric* channels, i.e. those in which the received signal depends more on temperature and humidity of the atmospheric air than on surface properties. The rest of the channels, in which the bulk of the received radiation comes from the surface, are marked in Table 1 as window channels. However, it is worth noting that some of the atmospheric channels (15, 16, and 27–29) have significant contributions from the surface, which need to be taken into account in applications (for an example, see Sect. 7.2 below, item 2 therein).

For some more information on MTVZA-GY, see (Gorobets et al. 2007; Cherny et al. 2010) and the WMO (World Meteorological Organization), OSCAR (Observing Systems Capability Analysis and Review Tool) web site.

3. MTVZA-GY Atmospheric Channels

In this section, we briefly describe how the MTVZA-GY atmospheric channels depend on atmospheric temperature and humidity. These dependencies are modeled by the *forward model* $\mathcal{H}$ (RTTOV in this work) that maps the atmospheric profiles (vectors) of temperature $\mathbf{T}$ and humidity $\mathbf{q}$ to the brightness temperature T_b measured by the satellite sensor in the frequency channel in question. Neglecting other relatively minor contributors to the observed radiance and in the absence of heavily precipitating clouds, we write $T_b = \mathcal{H}(\mathbf{T}, \mathbf{q})$.

Sensitivities of T_b in a particular channel to $\mathbf{T}$ and $\mathbf{q}$ are quantified by the vectors of partial derivatives $\partial T_b/\partial \mathbf{T} = \partial \mathcal{H}(\mathbf{T}, \mathbf{q})/\partial \mathbf{T}$ and $\partial T_b/\partial \mathbf{q} = \partial \mathcal{H}(\mathbf{T}, \mathbf{q})/\partial \mathbf{q}$, respectively, often called Jacobians.

To compute the simulated brightness temperatures and the Jacobians in the MTVZA-GY channels, the RTTOV model was fed with operational 6 h National Centers for Environmental Prediction (NCEP) Global Forecast System (GFS) forecasts. Both the 6 h forecast and the simulated T_b (computed from the 6 h forecasts) are called *background* in what follows.

3.1. Temperature Channels

MTVZA-GY channels 15–24 depend primarily on atmospheric temperature. Figure 2 shows the Jacobians for temperature sounding channels computed at an arbitrarily selected sub-satellite point located in the mid-latitude ocean with the geographic and time coordinates indicated in the title of the plots (in the format yyyymmddhh).

The left panel of Fig. 2 displays the Jacobians with their maxima in the troposphere (tropospheric channels). The right panel of Fig. 2 depicts the Jacobians for the stratospheric channels. The passbands of the channels have been selected by the instrument designers in the lower-frequency wing of the 60-GHz oxygen absorption band in such a way that the higher the channel number, the more opaque the channel and, therefore, the higher the Jacobian's maximum.

In temperature channels, the dependence on $\mathbf{T}$ is largely linear and the dependence on $\mathbf{q}$ is weak, so that the temperature channels' Jacobians do not exhibit significant changes at different points in the horizontal and in time (not shown).

3.2. Humidity Channels

Channels 27–29 are sensitive primarily to atmospheric water vapor (and to temperature as well), with the sensitivity to $\mathbf{T}$ being largely linear, whilst the sensitivity to $\mathbf{q}$ being significantly non-linear.

Figure 3 shows humidity sounding channels' Jacobians: with respect to atmospheric temperature (left panels) and specific humidity (right panels), at a high-latitude point (upper panels) and a low-latitude point (lower panels). The Jacobians were computed by RTTOV for the background fields valid at the day and time indicated in the title of the plot.

In Fig. 3, one can see that $\partial T_b/\partial \mathbf{T}$ is always positive, whereas $\partial T_b/\partial \mathbf{q}$ is mainly negative. The positivity of $\partial T_b/\partial \mathbf{T}$ is due to the fact that the emitted radiation grows with temperature following the Planck law whereas absorption is, in the first approximation, independent of the absorber's temperature. The negativity of $\partial T_b/\partial \mathbf{q}$ can be reproduced in the solution of the radiative transfer equation in the absence of scattering if the absorption is high enough (not shown). If the optical depth of the atmospheric profile is low (e.g., in cold conditions and/or over high terrain), then $\partial T_b/\partial \mathbf{q}$ for a humidity sounding channel can become positive, as it is the case for channel 27 in Fig. 3b.

Another feature of the Jacobians seen in Fig. 3 is that the larger the channel number, the higher the maximum in $\partial T_b/\partial \mathbf{T}$ (see the left panels of Fig. 3). This can be explained as follows. The passbands of the three humidity channels are all centered at the frequency that corresponds to the maximum absorption in the 183 GHz water vapor line, with the passband width decreasing with the channel number (see Table 1). This implies that the mean (over the passband) absorption increases with the channel number, which, in turn, shifts the maximum of the Jacobian with respect to temperature to a higher altitude. This shift is, however, not pronounced in the Jacobians with respect to humidity (see the right panels of Fig. 3).

E.g., Comparing Figs. 3 and 2 shows that the Jacobians in humidity sounding channels are

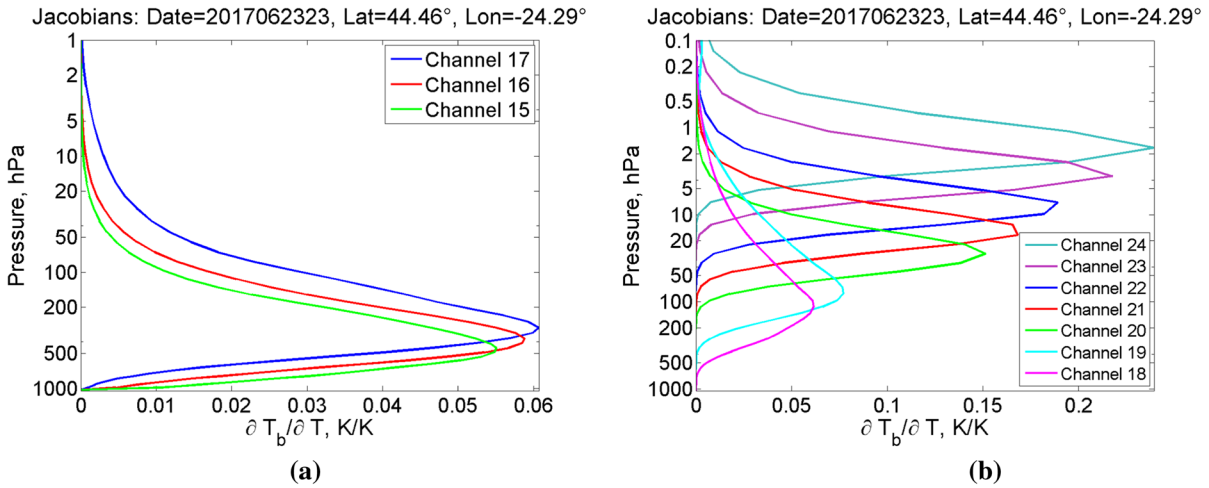

Figure 2
Jacobians of atmospheric *temperature* sounding channels: **a** tropospheric channels, **b** stratospheric channels

significantly *less smooth* in the vertical than in temperature channels. To explain this behavior, we recall that the temperature channels are in an *oxygen* absorption band whereas the humidity channels are in a *water vapor* absorption line. It is well known that oxygen is a well-mixed gas in the atmosphere whereas water vapor is not (e.g., Randall 2012). It is the spatial uniformity of oxygen and the linearity of the dependence of T_b on **T** that leads to the smoothness of the temperature channels' Jacobians, and it is the spatial non-uniformity of the water vapor concentration together with the non-linearity of the dependence of T_b on **q** that cause the irregular behavior of the humidity channels' Jacobians in the vertical.

This effect also causes a greater *horizontal* variability in the Jacobians in humidity sounding channels. For example, the Jacobians computed at a high-latitude point (the upper panels of Fig. 3) are sensitive to significantly lower parts of the atmosphere as compared to the Jacobians computed at a low-latitude point (the lower panels of Fig. 3). This can be understood by noting that at low latitudes the atmosphere is significantly warmer; therefore, it normally contains much more water vapor so that the optical depth in the H_2O absorption line is greater, which, as discussed above, raises the Jacobians (the more optically thick the absorbing layer in the atmosphere, the less "visible" for the radiometer its lower part becomes).

Finally, we remark that the MTVZA-GY frequency channels partly coincide with or are close to channels of the following instruments: Special Sensor Microwave Imager/Sounder (SSMIS) (Kunkee et al. 2008), Advanced Microwave Sounding Unit-A (AMSU-A), Advanced Microwave Sounding Unit-B (AMSU-B), MHS (Microwave Humidity Sounder) (Weng et al. 2003, see also Table 4 below), and Advanced Technology Microwave Sounder (ATMS) (Weng et al. 2012).

4. Motivation

MTVZA-GY data undergo an on-orbit radiometric calibration in which two targets are used: the cold space (with the temperature of the cosmic microwave background of about 2.73 K) and a black body warm target (with the temperature of about 250 K). This two-point instrument calibration technique converts the electric signal from the antenna to the antenna brightness temperature T_a. However, soon after launch large global and airmass-dependent biases in antenna temperatures were found. Significant ascending-descending bias differences and striping noise (larger along-track variability as compared to the across-track variability in the data) were also observed (Uspensky et al. 2015). Differences in the assumed and true passbands were hypothesized as a

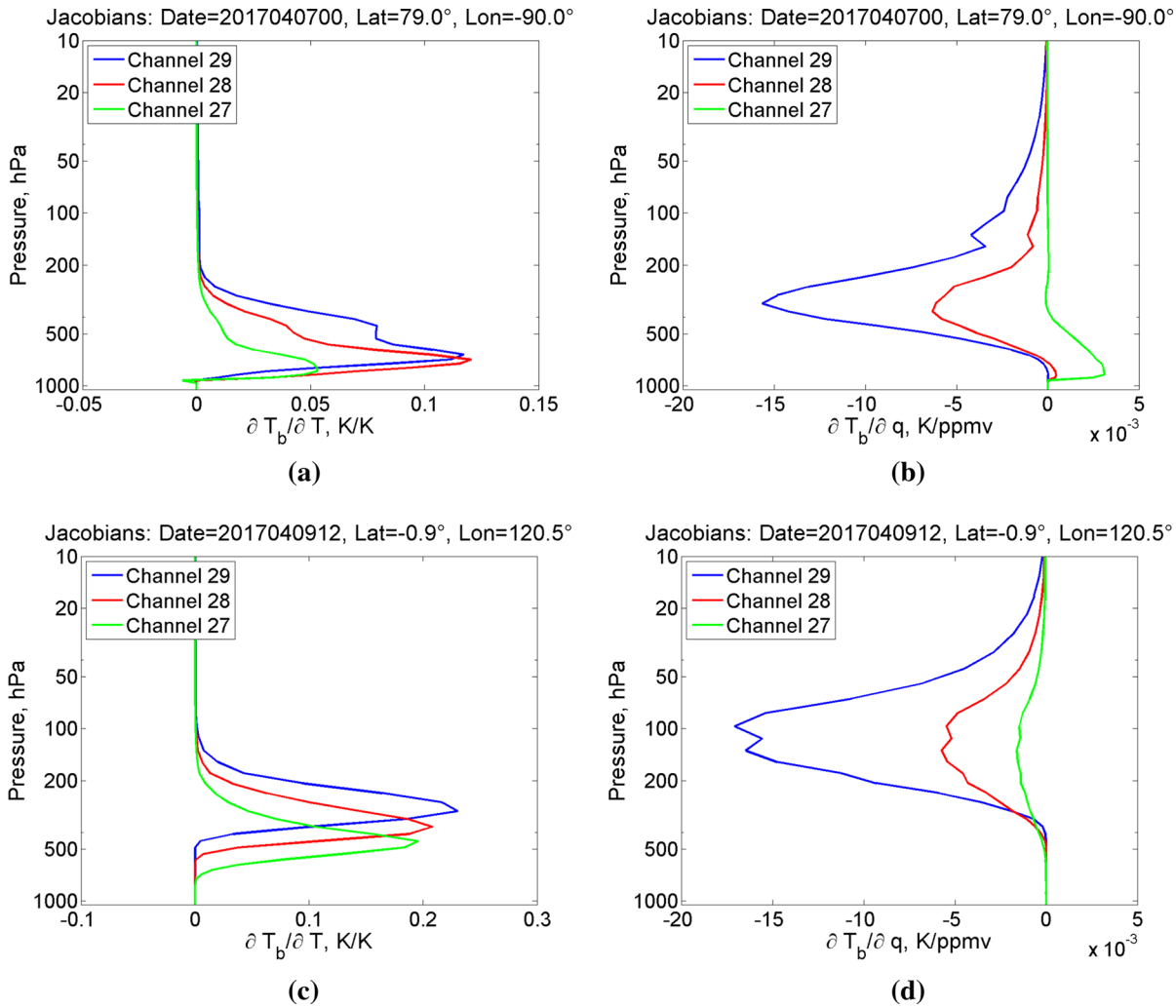

Figure 3
Jacobians of atmospheric *humidity* sounding channels: left: with respect to atmospheric temperature, right: with respect to atmospheric humidity, upper: at a high-latitude observation point, lower: at a low-latitude observation point

possible source of large errors. Another reason for large and varying biases could be radiometric calibration issues.

To reduce the errors/biases, Uspensky et al. (2015), see also Uspensky et al. (2017), developed a recalibration algorithm based on the linear regression:

$$T_{\mathrm{b}} = aT_{\mathrm{a}} + b, \tag{1}$$

where T_{b} is the recalibrated brightness temperature, and a and b are the regression coefficients (estimated from a training sample). The recalibrated and bias-corrected (following Harris and Kelly 2001) MTVZA-GY data were assimilated by Gayfulin et al. (2017) in the meteorological data assimilation system of the HydroMetCentre of Russia. A significantly positive impact of MTVZA-GY observations in the Southern Hemisphere in the absence of AMSU-A observations was found. However, it has been felt that further improvements in the recalibration technique were possible.

We started this study by examining uncorrected antenna temperatures as reported in raw (level-1b) data files. The observations were then compared with

the background (defined at the beginning of Sect. 3). The resulting biases and standard deviations averaged over three two-week periods in 2017 (for details, including the choice of the channels, see Sect. 7.1 below) are presented in Table 2. One can see that the data indeed suffered from very large biases and relatively large standard deviations.

Then, we reproduced results obtained by Uspensky et al. (2017), that is, we corrected antenna temperatures using Eq. (1) (this procedure is referred to in what follows as "simple correction"). As compared with the background, the remaining biases appeared to be quite large, exhibiting a kind of systematic behavior. Specifically, Fig. 4a shows the geographic distributions of local biases for channel 18 for an arbitrarily chosen 30 h period indicated in the figure caption. The local biases were computed by averaging observation-minus-background (OmB) deviations over $3^\circ \times 3^\circ$ grid cells of the regular latitude–longitude grid on the globe.

The complexity of the geographic distributions of the local biases in Fig. 4a, which goes beyond a latitudinal dependence, and a kind of systematic pattern seen in this figure, which clearly cannot be explained by air-mass dependence, suggest that the main cause of the biases is not related to the atmosphere or to the surface. On the other hand, it has been reported by several authors that *solar radiation* can cause significant biases in microwave satellite data (Bell et al. 2008; Wessel et al. 2008; Kunkee et al. 2008; Geer et al. 2010; Zou and Wang 2011). For these reasons, we decided to examine MTVZA-GY errors as functions of the azimuth and zenith solar angles (available for each pixel and denoted here by α and ζ, respectively).

The resulting dependence of the local biases on the solar angles is presented in Fig. 4b where the local biases were computed by averaging OmB deviations over cells of the $2^\circ \times 2^\circ$ grid on the α–ζ plane (cf. Fig. 4 in Bell et al. (2008)). It is seen that on the α–ζ plane, the local bias field is much smoother and "simpler", which is indicative of the existence of a direct link of the biases to the solar angles. On the other hand, the "simpler" and smoother pattern of the local biases on the α–ζ plane is easier to handle. This led us to develop a Solar Angles dependent bias Correction (SAC) procedure aimed at the removal of the local bias pattern on the α–ζ plane. The procedure is described below in Sect. 6.

5. *Existing Approaches to Post-launch Calibration of Microwave Radiometers*

Post-launch calibration/correction is a standard procedure employed for new satellite observation types. It is performed by comparing new observations with other (reference) data whose accuracy is more or less known. From the comparison, a *correction model* is developed and then applied to new data in order to increase their accuracy.

Kunkee et al. (2008) compared brightness temperatures in lower atmospheric SSMIS channels with European Centre for Medium-Range Weather Forecasts (ECMWF) analyses, radiosonde profiles, and additional campaign data described in Wessel et al. (2008). Wessel et al. (2008) used dedicated high-quality RS-90 Vaisala radiosonde launches, a water vapor Raman lidar, and high-altitude Rayleigh lidar data as a reference. Bell et al. (2008), Kunkee et al. (2008) and Wessel et al. (2008) identified the role of solar heating for SSMIS and performed reflector emission corrections.

Swadley et al. (2008) calibrated observations in upper atmospheric SSMIS channels (with the main contribution from the stratosphere and mesosphere) using ECMWF analyses below 40 km altitude merged with temperature observations in the altitude range 40–80 km from three Rayleigh lidars and appended with Committee on Space Research

Table 2

Deviations of uncorrected observations from the background, K

Sensor/scheme	Ch15	Ch16	Ch17	Ch18	Ch19	Ch20	Ch27	Ch28	Ch29
MTVZA/raw data (bias)	− 7.5	− 13.2	− 15.1	− 13.5	− 6.6	− 9.9	− 18.3	− 18.7	− 13.3
MTVZA/raw data (st.dev.)	0.74	1.56	2.76	0.63	0.90	0.92	2.17	2.18	3.51

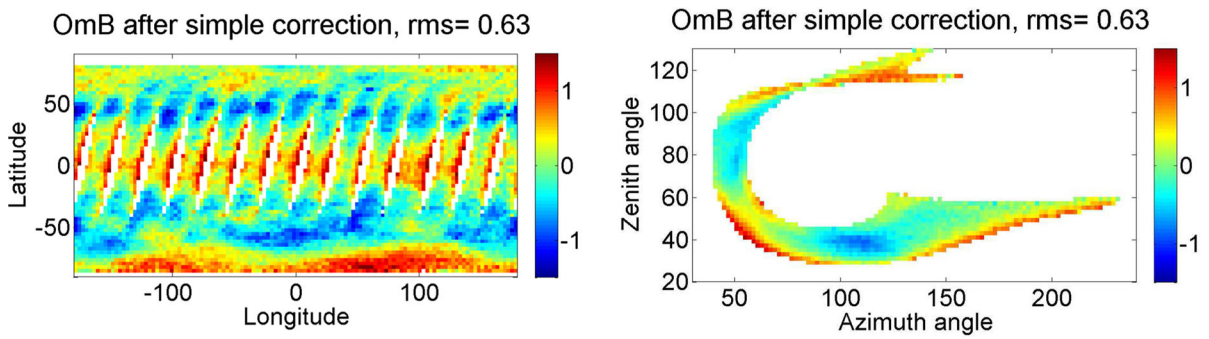

Figure 4
Local biases after "simple correction" for observations from 21 h UTC, 12 June 2017 to 3 h UTC, 14 June 2017 (descending orbits): **a** on the geographic map. **b** On the α–ζ plane

International Reference Atmosphere (CIRA) and Mass Spectrometer and Incoherent Scatter (MSIS) atmosphere model data above 80 km. They introduced a Doppler shift (induced by the spacecraft velocity) compensation and empirically modified an oxygen absorption linewidth parameter in the radiative transfer model to reduce the biases.

Zou and Wang (2011) intercalibrated AMSU-A observations on board several polar orbiting satellites using simultaneous nadir overpasses and global ocean mean differences.

Zou et al. (2014) removed scan-position-dependent biases in ATMS observations. The biases were computed by comparing raw ATMS data with Global Positioning System (GPS) radio occultation data converted to brightness temperatures using a radiative transfer model.

6. The Solar Angles Dependent Bias Correction Technique (SAC)

6.1. Setup

To avoid costly observation campaigns and reliance on other satellites for operational recalibration/correction, we decided to utilize the background (see Sect. 3) as the reference.

In the sequel, it is assumed that MTVZA-GY observation data are grouped in batches according to the actual measurement time. One batch consists of observations with the measurement time within a 6 h time window centered at 0, 6, 12, and 18 UTC.

The vector of observations (antenna temperatures T_a) in a 6 h time window is denoted by **y** and the vector of the respective RTTOV simulated (i.e. background) brightness temperatures by **z**. The length of both vectors **y** and **z** is equal to the number of observations in the time window, n_{obs}. Data assimilation terminology and methodology are extensively used in the rest of this section.

6.2. Correction Model

By a correction model, we understand a mapping of antenna temperatures T_a to corrected/recalibrated higher-quality brightness temperatures T_b.

In our case, to account for the solar angles, we let the two coefficients, a and b, of the simple correction scheme Eq. (1) be functions of α and ζ:

$$T_b = a(\alpha, \zeta) \cdot T_a + b(\alpha, \zeta). \tag{2}$$

This model is discretized by introducing a grid, $G_{\alpha\zeta}$ (with the number of points n_{grid}), in the α–ζ plane. $G_{\alpha\zeta}$ spans all plausible values of α and ζ. The values of the *coefficient fields* $a(\alpha, \zeta)$ and $b(\alpha, \zeta)$ on the grid $G_{\alpha\zeta}$ are collected in the respective vectors **a** and **b** (both of length n_{grid}).

Further, in order to apply the coefficient fields **a** and **b** (the n_{obs}-vectors) defined on a discrete grid of solar angles to the n_{obs}-vector of observations **y** with arbitrary solar angles, we introduce the *observation*

operator **H**. The $n_{\mathrm{obs}} \times n_{\mathrm{grid}}$ matrix **H** is designed in such a way that its application to vectors **a** and **b** results in their *interpolation* from the grid $G_{\alpha\zeta}$ they are defined on to the observation points α_i and ζ_i (with $i = 1, 2, \ldots, n_{\mathrm{obs}}$). In other words, the values of the fields a and b (represented by the vectors **a** and **b**) at the observation point i are $(\mathbf{Ha})_i$ and $(\mathbf{Hb})_i$, respectively. The interpolation is taken to be the simplest one: piecewise constant so that in the ith row of **H** there is only one entry equal to 1 (which corresponds to the grid point closest to the location of the ith observation) with all other entries equal to 0.

To represent the pointwise multiplication of $a(\alpha, \zeta)$ by T_{a} in Eq. (2) at all observation points in the vector–matrix form, we, finally, introduce the $n_{\mathrm{obs}} \times n_{\mathrm{obs}}$ matrix $\mathbf{Y} = \mathsf{diag}\,(\mathbf{y})$, where $\mathsf{diag}\,(\mathbf{y})$ stands for the diagonal matrix with the n_{obs}-vector of observed antenna temperatures **y** on its main diagonal. With this matrix, the correction model Eq. (2) can be rewritten as follows:

$$\widetilde{\mathbf{y}} = \mathbf{YHa} + \mathbf{Hb}, \tag{3}$$

where $\widetilde{\mathbf{y}}$ is the n_{obs}-vector of corrected observations.

This completes the description of our main solar angles dependent correction model. The gridded two-dimensional coefficient fields **a** and **b** (i.e. the SAC model parameters) need to be estimated.

6.3. *Variational Estimation of the Coefficient Fields* **a** *and* **b**

We start by stating that, first of all, our correction model, Eq. (3), has to *fit the data*, that is, **a** and **b** should be such that in each 6 h-window batch, the corrected observations $\widetilde{\mathbf{y}}$ be close to the respective reference data vector **z** (closer than the antenna temperatures **y**). In other words, we seek to minimize the *observation misfit*

$$J_{\mathrm{obs}}(\mathbf{a}, \mathbf{b}) = \|\widetilde{\mathbf{y}} - \mathbf{z}\|^2 = \|\mathbf{YHa} + \mathbf{Hb} - \mathbf{z}\|^2, \tag{4}$$

where $\|.\|$ denotes the ordinary quadratic vector norm (the square root of the sum of squares of all vector entries). However, the naive optimization problem $J_{\mathrm{obs}}(\mathbf{a}, \mathbf{b}) \rightarrow \min$ would be, clearly, ill-posed because observations are, normally, not available in *all* grid cells so that nothing would constrain (in this formulation) the functions $a(\alpha, \zeta)$ and $b(\alpha, \zeta)$ at the non-observed grid points (i.e. where there are no observations in the four neighboring grid cells).

To make the problem well posed, we have to *regularize* it by introducing *additional (prior) information* on the fields in question, **a** and **b**. We do this as follows. First, we assume that for each 6 h time window, there are *first guess* fields $\mathbf{a}^-$ and $\mathbf{b}^-$ (defined on $G_{\alpha\zeta}$) from which the estimates **a** and **b** should be "not too far" (this constitutes the *first-guess constraint*). Second, we postulate that the estimated fields **a** and **b** should be smooth as functions of the two solar angles (this is the *smoothness constraint*).

The first-guess constraint is imposed by penalizing deviations of **a** and **b** from $\mathbf{a}^-$ and $\mathbf{b}^-$, respectively:

$$J_{\mathrm{fg}}(\mathbf{a}, \mathbf{b}) = w_{\mathrm{a}}^2 \|\mathbf{a} - \mathbf{a}^-\|^2 + w_{\mathrm{b}}^2 \|\mathbf{b} - \mathbf{b}^-\|^2, \tag{5}$$

where w_{a} and w_{b} are the weights (parameters).

The smoothness constraint is imposed by penalizing the magnitude of the gradients of the (gridded) functions $a(\alpha, \zeta)$ and $b(\alpha, \zeta)$:

$$J_{\mathrm{smo}}(\mathbf{a}, \mathbf{b}) = w_{\mathrm{a}}^2 L^2 \|\mathbf{Ga}\|^2 + w_{\mathrm{b}}^2 L^2 \|\mathbf{Gb}\|^2. \tag{6}$$

Here, **G** is the $2n_{\mathrm{grid}} \times n_{\mathrm{grid}}$ matrix that represents the gridded version of the gradient[3] and L denotes the desired *length scale* of the coefficient fields **a** and **b** on the α–ζ plane.

To summarize, we wish the estimates of **a** and **b**, which will also be called the *updated fields* $\mathbf{a}^+$ and $\mathbf{b}^+$, to minimize both the observation misfit J_{obs}, Eq. (4), and the two penalties, the first-guess penalty J_{fg}, Eq. (5), and the smoothness penalty J_{smo}, Eq. (6). Formally, the updated fields $\mathbf{a}^+$ and $\mathbf{b}^+$ are sought as a solution to the following variational optimization problem:

$$J(\mathbf{a}, \mathbf{b}) = J_{\mathrm{obs}}(\mathbf{a}, \mathbf{b}) + J_{\mathrm{fg}}(\mathbf{a}, \mathbf{b}) + J_{\mathrm{smo}}(\mathbf{a}, \mathbf{b}) \rightarrow \min. \tag{7}$$

The optimization problem Eq. (7), in which the three terms are defined in Eqs. (4)–(6), is a quadratic one. Besides, it is straightforward to show that the presence of the first-guess term J_{fg} indeed regularizes the

[3] The $2n_{\mathrm{grid}}$ rows of the matrix **G** account for the two directed finite differences at each grid point: one in the α direction and the other in the ζ direction.

problem so that $J_{\text{obs}}(\mathbf{a}, \mathbf{b})$ is a strictly convex function. This guarantees that there is a unique minimum of J easily found by differentiating J with respect to the entries of $\mathbf{a}$ and $\mathbf{b}$, equating the respective derivatives to zero, and solving the resulting system of linear algebraic equations (technical details and the resulting system of linear equations are omitted). A conjugate gradient solver with sparse matrix algebra is adopted from the meteorological data assimilation system of the Hydrometcenter of Russia (outlined by Gayfulin et al. 2017).

It is worth noting at this point that the above variational scheme is decoupled from a meteorological analysis and, thus, is different from the Variational Bias Correction scheme (e.g., Dee and Uppala 2009).

6.4. Sequential Cycling

To provide the above variational scheme with the first-guess fields $\mathbf{a}^-$ and $\mathbf{b}^-$ we employ the sequential cycling approach widely known in data assimilation as the "analysis-forecast" cycle (e.g., Daley 1997), in which the first guess is computed from the previous analysis.

As noted in Sect. 6.1, the data are divided into non-overlapping portions $(\mathbf{y}_t, \mathbf{z}_t)$ for consecutive 6 h time windows $t = 0, 1, 2, \ldots$. The estimation process consists of the following steps.

1. At the start of the estimation process, i.e. at the time step $t = 0$ (the so-called "cold start") the constant (on the α–ζ plane) fields $\mathbf{a}_0$ and $\mathbf{b}_0$ are specified by solving (using ordinary least-squares) the quadratic optimization problem

$$\|a\mathbf{y} + b\mathbf{1} - \mathbf{z}\|^2 \to \min, \tag{8}$$

where a and b are the two numbers and $\mathbf{1}$ stands for the n_{grid}-vector whose all entries are equal to 1. The resulting fields $\mathbf{a}_0^+ = a\mathbf{1}$ and $\mathbf{b}_0^+ = b\mathbf{1}$ are the initial updated fields.

2. For $t = 1, 2, \ldots$, the previous-time-step updated fields $\mathbf{a}_{t-1}^+$ and $\mathbf{b}_{t-1}^+$ are propagated forward in time using the simplest *persistence forecast* (because nothing definitely better is available to predict/extrapolate in time the coefficient fields $\mathbf{a}$ and $\mathbf{b}$). The result is the next-time-step *first guess* fields

$$\mathbf{a}_t^- = \mathbf{a}_{t-1}^+ \quad \text{and} \quad \mathbf{b}_t^- = \mathbf{b}_{t-1}^+. \tag{9}$$

3. The variational estimation of the fields $\mathbf{a}_t$ and $\mathbf{b}_t$ is performed following Sect. 6.3, producing the updated fields $\mathbf{a}_t^+$ and $\mathbf{b}_t^+$.

This cyclic update process is repeated in time as long as needed (just like in any operational meteorological or oceanographic data assimilation system). As a result, at time step t, we have the fields $\mathbf{a}_t^-$ and $\mathbf{b}_t^-$ adaptively estimated using *past* data. These fields are applied to *current* observation data $\mathbf{y}_t$ giving rise to the final bias corrected observations $\widetilde{\mathbf{y}}_t$, which are, then, ready to be used in a meteorological data assimilation system or for other purposes (and whose accuracy will be examined in Sect. 7 below). Note that using the $\mathbf{a}_t^-$ and $\mathbf{b}_t^-$ fields *not* affected by the *current* meteorological forecast is safe, in the sense that the forecast is *not* used twice in a meteorological data assimilation system.

The three parameters w_{a}, w_{b}, and L of the variational estimation scheme are subject to (channel-dependent) tuning.

6.5. Diurnal Cycle

Experimentally, we found that the local biases appear to exhibit a kind of *diurnal cycle* (besides the solar-angles dependence), so that a bias field on the α–ζ plane appears to be more similar to the bias field 24 h ago than to the bias field 6 h ago (not shown). This means that the 24 h persistence forecast would be more accurate in predicting the current coefficient fields $\mathbf{a}$ and $\mathbf{b}$ than the above 6 h persistence forecast.

To account for this feature, we introduced four independent cyclic update processes described above (instead of one). The 1st process assimilates raw observations and produces the coefficient fields $\mathbf{a}$ and $\mathbf{b}$ at the time instances $0, 4, 8, \ldots$ (i.e. every 24 h). The 2nd process does the same job at the time instances $1, 5, 9, \ldots$, etc. Each cyclic update process still assimilates observations in 6 h batches but the batches are now 24 h apart, so that the 24 h persistence is used as the first guess:

$$\mathbf{a}_t^- = \mathbf{a}_{t-4}^+ \quad \text{and} \quad \mathbf{b}_t^- = \mathbf{b}_{t-4}^+. \tag{10}$$

In this procedure, there are four "cold starts" (see item 1 in the list in Sect. 6.4), one per each of the four independent cyclic update processes.

6.6. Simpler Correction Techniques Used for Comparison

Our main SAC technique described above in this section is compared in Sect. 7 with two simpler techniques. The "simple" one was introduced in Sect. 4 and uses constant in time scalar recalibration coefficients a and b computed once at the beginning of the correction period by solving the problem Eq. (8).

The other simpler technique (referred to as the "evolving simple" in what follows) solves the problem Eq. (8) at each time step independently and then performs the temporal "on-line" smoothing of the resulting coefficients a_t and b_t [with the 24 h cycle, as in Eq. (10)]:

$$a_t^+ = \mu a_{t-4}^+ + (1-\mu)a_t \qquad \text{and} \qquad b_t^+ = \mu b_{t-4}^+ + (1-\mu)b_t, \tag{11}$$

where μ is the real number that controls the degree of smoothing. The resulting updated coefficient fields are $\mathbf{a}_t^+ = a_t^+\mathbf{1}$ and $\mathbf{b}_t^+ = b_t^+\mathbf{1}$. The smoothing parameter μ is to be tuned for each channel.

7. Numerical Experiments

In this section, we validate MTZVA-GY observations corrected with the three techniques: the main solar angles dependent correction technique (SAC, see Sects. 6.2–6.5), the "simple" one with constant in space and time coefficients a and b, and the "evolving simple" one, in which the coefficients a and b are constant in space but evolve in time (the two latter techniques are described in Sect. 6.6). The accuracy of corrected MTVZA-GY observations is evaluated by comparing them with the background.

It is worth stressing that the corrected observations are compared with *independent* background data. Indeed, as noted at the end of Sect. 6.4, the corrected observations $\widetilde{\mathbf{y}}_t$ are computed with the correction coefficients/fields estimated using *past* data and *past* backgrounds $\mathbf{z}_{t-1}, \mathbf{z}_{t-2}, \ldots$.

7.1. Data and Experimental Setup

Data from three 2-week time periods in 2017 were examined: 7–20 February, 7–20 April, and 7–20 June.[4] Atmospheric temperature channels 15–20 and humidity channels 27–29 were tested. Temperature sounding channels above channel 20 were not tested because the background fields were available to us only up to 10 hPa. The horizontal resolution of the background fields (see Sect. 3) was 0.5°. In the vertical, the background fields had 26 levels from 1000 to 10 hPa.

Observation data were available in HDF4 format. The data files contained the following information for each pixel: observation time, latitude and longitude of the sub-satellite observation point (seen by the sensor's antenna), the two solar angles, an indicator of the type of the underlying surface (not used), and the observed antenna brightness temperatures for the 24 available frequency channels listed in Table 1.

The background fields were interpolated (both in space and time) to sub-satellite points. The time interpolation, also known as FGAT (first guess at appropriate time), was performed from three forecasts with 0, 6, and 12 h lead time, all started 6 h earlier than the center of the current observation window.

It is worth noting at this point that we preferred the meteorological short-range *forecast* (background) to be used as the reference, not *analyses* as in Swadley et al. (2008), Kunkee et al. (2008) and Uspensky et al. (2017). This is because our intermittent correction and validation techniques are intended to work operationally, which requires that the operational reference fields be independent of the data to be corrected. If the validation technique utilized *analyses*, then, at some point in time, when (hopefully) MTVZA-GY observations are operationally assimilated, the validation technique would become flawed because the analysis would be dependent on current MTVZA-GY data and so not suitable as a reference for their bias correction.

[4] An initially selected period 1–15 August 2016 was rejected because abnormally large errors (1.5–2 times larger than normal) were observed in several channels on descending orbits during that period.

The resolution of the grid (on the α–ζ plane) on which the coefficient fields **a** and **b** were defined was 2°. The tuning parameters of the correction/recalibration schemes were selected by trial and error in preliminary experiments. It appeared to be sufficient to specify channel-independent parameter values, $w_a = 400$ K, $w_b = 4$, and $L = 3°$. The memory parameter μ in the "evolving simple" correction scheme was equal to 0.87, which corresponds to the smoothing time scale about 7 days.

For observations close to the North Pole, the azimuth (defined as the angle from the direction due north to the horizontal projection of the sun's rays, measured clockwise) becomes unstable, so the estimation of the coefficient fields is performed outside the polar cap north of 80N. The results below were computed for observations outside this polar cap.

7.2. Observation Selection and Quality Control

First, raw observations were subjected to a "buddy check" performed to reject single-pixel outliers. Each raw observation y_{ij} (where i labels the scan position and j the scan line) was compared with all its immediate neighbors, $y_{i\pm1,j}$ and $y_{i,j\pm1}$. If the absolute values of all the differences $y_{i\pm1,j} - y_{ij}$ and $y_{i,j\pm1} - y_{ij}$ were greater than 0.4 K in modulus for temperature channels and 1 K for humidity channels, then the observation y_{ij} was rejected for being unacceptably noisy.

After that, observations were thinned. Note that this is normally done in order to reduce the computational cost and to diminish the role of spatial error correlations (Gorin and Tsyrulnikov 2011) not accounted for in most data assimilation systems. Here, the data were thinned only to reduce the computational burden, so that the results below are applicable to all MTVZA-GY data. Each 5th observation in the scan line and each 5th scan line were retained for further processing. This implies that the resolution of the thinned dataset was $16 \times 5 = 80$ km in both the along-scan-line and the along-track directions.

Finally, a number of quality checks were applied as described below. If any of these checks failed, the observation was rejected.

1. *Background check* An observation was rejected if its departure from the background exceeded 2 K for all temperature sounding channels except for the poorest channel 17, exceeded 3 K for channel 17, and 8 K for humidity sounding channels.
2. *Surface check* Over land, the microwave soil emissivity depends on many poorly known factors such as vegetation and soil wetness (Prigent et al. 2006). Similarly, large variations in microwave sea-ice emissivity are well documented (e.g., Haggerty and Curry 2001). Therefore, observations that significantly depend on the surface properties over land and sea ice were rejected using the following simple rule. The sensitivity to the surface was approximated by the sensitivity to the surface temperature, i.e. by the partial derivative (available from RTTOV) of the observation T_b with respect to the surface temperature T_s. The observation was rejected if $\partial T_b/\partial T_s$ exceeded the empirically selected threshold of 0.1. This surface check was also applied over clear sea (where the uncertainty in the emissivity is lower but the emissivity itself is lower as well). Channels 15 and 27 were used only over clear sea. Note that, implicitly, the above surface check accounts for high terrain. The typical for the temperature sounding channel 16 and the humidity sounding channels dependence of OmB departures on $\partial T_b/\partial T_s$ over land is shown in Fig. 5 (channel 16, data were accumulated for the period 14–16 April 2017 from ascending orbits). The RMS (root-mean-square) curve was computed by nonparametric smoothing of individual OmB deviations on the OmB-vs-$\partial T_b/\partial T_s$ scatterplot. It is seen that the RMS curve grows (implying growing observation errors) with the increasing $\partial T_b/\partial T_s$. The rejection rule $\partial T_b/\partial T_s > 0.1$ was selected as an informal compromise between the quality of retained observations (indicated by the RMS curve) and their number (indicated by the cumulative distribution function curve, see the figure caption).
3. *Heavy rain check* Finally, observations in all channels were rejected in heavily precipitating cloud areas. The rejection criterion compared the liquid water path computed from the accumulated 6 h rainfall forecast (available in the background)

with the threshold of 0.05 kg/m^2 (Weng et al. 2012). It is worth noting at this point that the rainfall estimated from *observed* brightness temperatures in different window channels of the same sensor would be useful here. E.g., Ferraro and Marks (1995) used for this purpose a Scattering Index defined as the difference of a high-frequency microwave channel (which is sensitive to precipitating ice particles and raindrops) and a combination of two low-frequency (and thus less sensitive to precipitation) microwave channels. However, we refrained from using that technique because some of the low-frequency and high-frequency microwave MTVZA-GY channels (marked as *window* in Table 1) are not available while others suffer from large errors, whose correction was beyond the scope of this study.

Rejection rates due to the application of the above four checks are given in Table 3 (note that the total rate may be less than the sum of the individual rates). One can see that in the higher peaking temperature channels and in the highest humidity channel 29, the largest portion of outliers was removed by the background check. The surface check was useful in rejecting outlying observations in the lower peaking temperature channel 16 and in the humidity channels. Note that the surface check behaved differently in the lowest channels 15 and 27, which were examined only over clear sea. It rejected no data in the *temperature* channel 15 but it rejected as much as 3.7% of data in the *humidity* channel 27. The reason of this difference is the stability of the Jacobians (weighting functions) in temperature channels (see Sect. 3.1), on the one hand, and the significant variability of the weighting functions in humidity channels (see Sect. 3.2), on the other hand. Specifically, $\partial T_b/\partial T_s$ in channel 15 was almost always below the 0.1 threshold, whereas channel 27 often became very low-peaking at high latitudes (see Fig. 3b as an example), which resulted in rejections of some observations over clear sea.

The buddy check rejected larger amounts of data in humidity channels than in temperature channels (because humidity is a more variable field than temperature and because the effective horizontal resolution for humidity channels is higher than for temperature channels, see the "FOV" and "Pixel" columns in Table 1). The heavy rain check was the least effective in removing outliers. Overall, the rejection rates in humidity channels were somewhat higher than in temperature channels.

In general, the quality of the MTVZA-GY data we studied was reasonably stable, but from time to time we observed sporadic spikes (hours and days long) in the error magnitude. Sometimes, the spikes were attributed to radio-frequency interference. The data flow was also quite stable, with relatively rare periods of missing data.

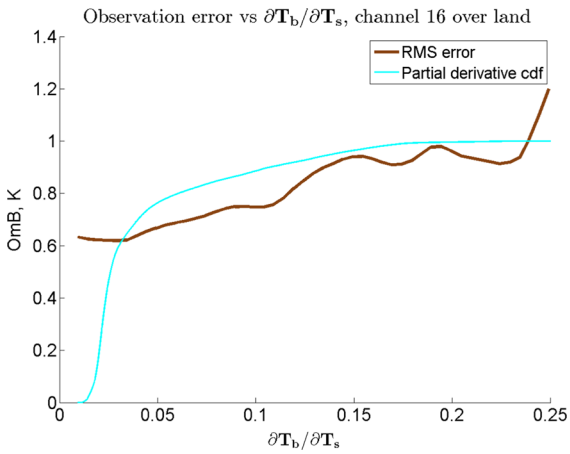

Figure 5
Dependence of observation-minus-background (OmB, K) departures on $\partial T_b/\partial T_s$. In the legend, "Partial derivative cdf" denotes the cumulative distribution function (which shows the portion of the data points with $\partial T_b/\partial T_s$ lower than the abscissa)

Table 3

Rejection rates due to the checks applied,%

Channel	Background check	Surface check	Buddy check	Heavy rain check	Total
15	2.2	0[a]	0.5	< 0.1	2.4
16	2.8	3.6	0.1	< 0.1	5.3
17	11.0	0.1	< 0.1	< 0.1	11.1
18	0.5	0	< 0.1	< 0.1	0.5
19	0.7	0	< 0.1	< 0.1	0.8
20	0.9	0	< 0.1	< 0.1	0.9
27	3.2	3.7[a]	2.2	< 0.1	7.9
28	2.2	7.0	1.0	< 0.1	9.2
29	5.7	3.5	1.1	< 0.1	8.9

[a]Over clear sea only (recall that over land and over sea ice channels 15 and 27 were not used)

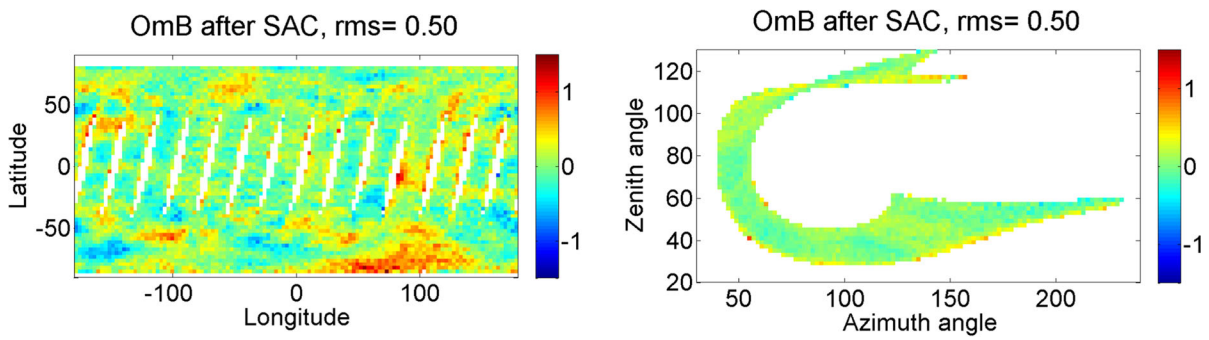

Figure 6
Local biases after SAC for observations from 21 h UTC, 12 June 2017 to 3 h UTC, 14 June 2017 (descending orbits). **a** On the geographic map. **b** On the α–ζ plane

7.3. Validation Results

7.3.1 Main Findings

Figure 6 shows the distributions of local biases of SAC-corrected observations in the same format as in Fig. 4. Comparing the two panels in Fig. 6 (the SAC scheme) with the two respective panels in Fig. 4 (the "simple" scheme) demonstrates how successfully the developed SAC scheme removes the local biases, leaving behind, largely, just noise. It is worth noting here that the residual noise on the geographic map, Fig. 6a, is stronger than on the α–ζ plane, Fig. 6b. This is because there are many more cells on the geographic grid populated by the observations, so that each cell is significantly less populated than a cell on the α–ζ plane, which implies greater sampling noise on the geographic grid.

Figure 7 shows the time series of biases and standard deviations of the OmB deviations for the three competing correction techniques. The season, the channel, and the orbit (descending) were selected in order to show the most typical results. One can see that the SAC significantly outperformed the "simple" and the "evolving simple" techniques. Noticeably, the improvement in the accuracy of SAC-corrected observations is predominantly in the standard deviation (the three upper curves). The global bias is easily removed by any of the three techniques. As for the two latter techniques, the "simple" one (in which, we recall, the coefficients a and b were constant both in space and time) turned out to be slightly inferior to the "evolving simple" technique (in which the coefficients a and b were constantly updated in time). In some other channels, the difference between the "simple" and the "evolving simple" techniques was larger and gradually increasing in time, as expected (not shown).

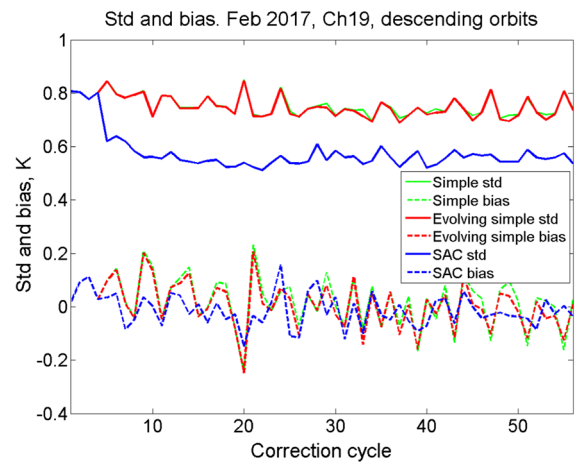

Figure 7
Biases and standard deviations of the OmB departures with the three correction schemes from 7 to 20 February 2017. Abscissa is correction cycles (consecutive 6 h time windows)

Finally, Table 4 displays the overall results: the RMS errors with respect to the background (averaged over the three time periods and over both ascending and descending orbits).[5] One can see that, indeed, the

[5] Note that in each two-week period, the first 24 h were not included in the averaging in order to let the cycling process reach its quasi-steady-state regime.

Table 4

Correction results. Deviations of corrected observations from the background, K

Sensor/scheme	Ch15	Ch16	Ch17	Ch18	Ch19	Ch20	Ch27	Ch28	Ch29
MTVZA/"Simple" (RMS)	0.72	0.85	1.76	0.62	0.71	0.80	2.46	2.60	3.52
MTVZA/"Evolving simple" (RMS)	0.67	0.83	1.70	0.62	0.71	0.79	2.35	2.51	3.34
MTVZA/**SAC** (RMS)	**0.56**	**0.63**	**1.04**	**0.50**	**0.56**	**0.62**	**2.24**	**2.38**	**3.12**
AMSU-A channel:	*Ch4*		*Ch5*	*Ch6*	*Ch8*	*Ch10*			
MHS channel:							*Ch5*	*Ch4*	*Ch3*
AMSU-A (RMS)	*0.56*		*0.36*	*0.29*	*0.34*	*0.34*			
MHS (RMS)							*1.58*	*1.56*	*1.57*

Results for the SAC-corrected MTVZA-GY data are indicated in bold face, whereas the results for the AMSU-A and MHS data (with "simple correction") are given in italic

SAC scheme significantly outperformed the two simpler competing techniques. And of course, the SAC corrected observations were much more accurate than antenna temperatures (whose accuracy is shown in Table 2 for the same set of observations as here). The comparison with AMSU-A and MHS is given below in Sect. 7.3.3.

The particularly poor performance of MTVZA-GY channel 17 is, most likely, caused by a significant difference between the assumed and the actual passbands, as hypothesized in Uspensky et al. (2015). The reason can be errors or shifts or drifts in the frequency of the local oscillator (Lu and Bell 2014).

7.3.2 Other Dependencies

Further investigation into the structure of remaining biases showed that the dependence of the RMS error on the scan position was significant only for the two simpler correction techniques and negligible for the SAC corrected data (not shown).

Seasonal differences in the accuracy of the SAC corrected MTVZA-GY observations were rather small (not shown). The differences between ascending and descending orbits also became insignificant after the introduction of the SAC.

7.3.3 Comparison with AMSU-A and MHS

AMSU-A and MHS data from Metop-A (which had virtually the same orbit as Meteor-M N2, whose data were studied in this research) during the above three time periods, were selected for comparison with MTVZA-GY observations. The AMSU-A and MHS data underwent the above "simple" correction procedure (to remove the state-independent part of the biases) and all the quality control checks in exactly the same way MTVZA-GY data did.

AMSU-A and MHS channels with similar passbands to the MTVZA-GY channels were examined. The results for the AMSU-A and MHS channels are presented in the lower part of Table 4. One can see that the only MTVZA-GY channel 15 had comparable accuracy to its AMSU-A counterpart, channel 4. The MTVZA-GY channel 17 had the worst performance, being some 3 times less precise than AMSU-A channel 5. The other MTVZA-GY channels appeared to be 1.5–2 times less accurate than their AMSU-A/MHS counterparts.

The magnitudes of OmB deviations for AMSU-A and MHS displayed in Table 4 are some 1.5 times greater than those reported by operational radiance data monitoring services (e.g., http://www.emc.ncep.noaa.gov/gmb/gdas/radiance/esafford/wopr/index.html). The primary reason for this difference is that here we performed no bias correction with airmass-dependent predictors [as in, e.g., Harris and Kelly (2001) or Dee and Uppala (2009)]. This was done in order to make the processing of AMSU-A and MHS data exactly the same as the processing of MTVZA-GY data. The secondary reason is that the background fields were available to us only up to 10 hPa.

It is worth noting that the comparison of MTVZA-GY vs. AMSU-A and MHS in terms of their respective deviations from the 6 h GFS forecast (used as the background in this study) seems to be not

entirely fair because AMSU-A and MHS are routinely assimilated into the GFS and so can be favored in this comparison. Even though it is the forecast and *not* the analysis that was used as the background, the observation errors of AMSU-A and MHS can be underestimated. To demonstrate this, we note that Gorin and Tsyrulnikov (2011) found that the AMSU-A observation error δy (where y denotes the observation and δ denotes the error) has two components, a spatio-temporally correlated component $\delta_c y$ (attributed to the radiative transfer model error) and the uncorrelated component $\delta_u y$ (attributed to the instrument measurement error). What is important for us here is that Gorin and Tsyrulnikov (2011) also found a positive *cross-correlation* κ between the correlated part of the satellite observation error $\delta_c y$ and the background error δz (where z stands for the 6 h forecast converted to brightness temperature).

We can easily write down the variance of the observation-minus-forecast increment: $\mathsf{Var}\,(y - z) = \mathsf{Var}\,(\delta_c y + \delta_u y - \delta z) = \mathsf{Var}\,\delta y + \mathsf{Var}\,\delta z - 2\kappa(\mathsf{Var}\,\delta_c y \cdot \mathsf{Var}\,\delta z)^{1/2}$. From this equation, it is seen that a positive κ indeed reduces the observation-minus-background variance. However, using the data from Table 1 in Gorin and Tsyrulnikov (2011), one can verify that the comparison of AMSU-A observations with GFS forecasts underestimated the real AMSU-A observation error standard deviation only by a few hundredths of a kelvin, which does not affect the general conclusion about the relative accuracy of MTVZA vs. AMSU-A data.

On the other hand, training the SAC scheme on *previous* background fields while examining against the *current* ones can lead to an underestimation of MTVZA-GY observation errors, too. This can take place if MTVZA-GY errors are correlated in time like AMSU-A errors. On balance, we believe that the above comparison of MTVZA-GY data vs. AMSU-A/MHS data for the same time periods is reasonably fair.

7.4. Remarks

1. In our SAC bias correction scheme, as in any other offline (decoupled) technique (e.g., Harris and Kelly 2001), a mapping of *background* errors into bias corrections can take place. We believe that this limitation of our approach is not of primary importance for the following reasons. First, errors and biases in MTVZA-GY data are much greater than errors and biases in the background. Therefore, the improvement in the observations accuracy due to our scheme strongly dominates any problem with the forecast-model bias. Second, our bias correction model is solar-angles dependent, whereas forecast biases are latitude, longitude, and air mass dependent (which should reduce the transfer of systematic errors from the forecast to the corrected observations). Third, our scheme can, in principle, be embedded in a variational bias correction scheme (e.g., Dee and Uppala 2009), in which the resulting observation bias is constrained not only by the meteorological forecast model but by other observation types as well.
2. A methodological comment. The relationship between the solar angles and the MTVZA-GY observation error we found is statistical and, as such, cannot guarantee that the solar radiation is indeed the only or even the dominant error source. Taking into account findings by other authors who studied the effect of solar heating on satellite microwave sensors in more detail (see the references in Sect. 4), we believe that the solar radiation is indeed an important error source for MTVZA-GY data. But we cannot exclude that our scheme may compensate for some other sources of error as well. E.g., any latitudinally dependent error can be aliased with the solar angles effect (because the solar angles exhibit a systematic change with latitude).

8. Conclusions

In this work, we have examined the accuracy of atmospheric temperature and humidity sounding channels of the conically scanning microwave radiometer MTVZA-GY on board the Meteor-M N2 satellite. Observation errors were measured by comparing observed brightness temperatures with their simulated counterparts. The simulated brightness temperatures were computed by the RTTOV radiative

transfer model applied to 6 h NCEP GFS forecast fields.

The observation biases were found to be dependent on the solar angles (zenith and azimuth). It appeared that a large portion of the observation error can be explained by a bias correction model that has an additive and a multiplicative component, both being smooth function of the two solar angles. This new solar angles dependent bias correction model was estimated using a sequential data assimilation (learning) algorithm with a variational observation update and a persistence-forecast time update.

Three two-week periods in summer, winter and spring/fall were selected for numerical experiments. The application of the estimated correction model to independent observations was shown to significantly improve their accuracy. The MTVZA-GY errors were compared with errors in the respective/similar channels of AMSU-A and MHS sensors for the same time periods.

As compared with the analysis in Uspensky et al. (2015), the errors in the corrected MTVZA-GY data have been substantially decreased. Differences in RMS errors between ascending and descending orbits are now insignificant. With the new correction scheme, the observation error magnitude is largely independent of the scan position. As compared with AMSU-A observations, corrected MTVZA-GY data in temperature sounding channels appear to be 1–3 times less accurate. In atmospheric humidity sounding channels, the corrected MTVZA-GY observations are about 1.5–2 times less precise than the MHS data.

In this work, no attempt was made to account for non-precipitating clouds. The striping noise phenomenon was not addressed either.

The MTVZA-GY radiometer on board Meteor-M N2 is not working properly since 15 August 2017. The next MTVZA-GY instrument is planned to be launched by the end of 2018. In total, 4–5 satellites of the Meteor-M type with the MTVZA-GY sensor on board are to be launched till 2025 in both the morning and the afternoon orbits.

Microwave observations from the current and future Meteor-M series satellites are expected to complement the existing constellation of polar orbiting meteorological satellites and contribute to the quality of numerical weather prediction and other meteorological technologies and studies.

Acknowledgements

The authors would like to thank I. V. Cherny for valuable discussions on various MTVZA-GY calibration issues. We are indebted to P. Rayer for extending the RTTOV model to include MTVZA-GY. S. A. Uspensky and N. S. Ekimov kindly provided raw data files and helped resolve technical issues with the files. We are also grateful to P. I. Svirenko, who provided us with the sparse-matrix conjugate gradient solver from the meteorological data assimilation system of the Hydrometcenter of Russia. The very helpful comments made by the two anonymous reviewers are gratefully acknowledged.

References

Asmus, V., Zagrebaev, V., Makridenko, L., Milekhin, O., Solovyev, V., Uspenskii, A., et al. (2014). Meteorological satellites based on Meteor-M polar orbiting platform. *Russian Meteorology and Hydrology*, *39*(12), 787–794.

Bell, W., English, S. J., Candy, B., Atkinson, N., Hilton, F., Baker, N., et al. (2008). The assimilation of SSMIS radiances in numerical weather prediction models. *IEEE Transactions on Geoscience and Remote Sensing*, *46*(4), 884–900.

Cherny, I. V., Mitnik, L. M., Mitnik, M. L., Uspensky, A. B., & Streltsov, A. M. (2010). On-orbit calibration of the Meteor-M microwave imager/sounder. In *IEEE International geoscience and remote sensing symposium (IGARSS)*, pp. 558–561. IEEE.

Daley, R. (1997). Atmospheric data assimilation. *Journal of the Meteorological Society of Japan Ser II*, *75*(1), 319–329.

Dee, D. P., & Uppala, S. (2009). Variational bias correction of satellite radiance data in the ERA-Interim reanalysis. *Quarterly Journal of the Royal Meteorological Society*, *135*(644), 1830–1841.

Ferraro, R. R., & Marks, G. F. (1995). The development of SSM/I rain-rate retrieval algorithms using ground-based radar measurements. *Journal of Atmospheric and Oceanic Technology*, *12*(4), 755–770.

Gayfulin, D., Tsyrulnikov, M., Uspensky, A., Kramchaninova, E., Uspensky, S., Svirenko, P., et al. (2017). The usage of MTVZA-GY a satellite microwave radiometer observations in the data assimilation system of the Hydrometcenter of Russia. *Russian Meteorology and Hydrology*, *42*(9), 564–573.

Geer, A. J., Bauer, P., & Bormann, N. (2010). Solar biases in microwave imager observations assimilated at ECMWF. *IEEE Transactions on Geoscience and Remote Sensing*, *48*(6), 2660–2669.

Gorin, V. E., & Tsyrulnikov, M. D. (2011). Estimation of multivariate observation-error statistics for AMSU-A data. *Monthly Weather Review*, *139*(12), 3765–3780.

Gorobets, N., Cherny, I., Chernyavsky, G., & Barsukov, I. (2007). Microwave imager/sounder MTVZA-GY of spacecraft Meteor-M. In: The sixth international Kharkov symposium on physics and engineering of microwaves, millimeter and submillimeter waves, June 25–30, 2007, vol. 2, pp. 772–774. IEEE.

Haggerty, J. A., & Curry, J. A. (2001). Variability of sea ice emissivity estimated from airborne passive microwave measurements during FIRE SHEBA. *Journal of Geophysical Research Atmospheres*, *106*(D14), 15265–15277.

Harris, B. A., & Kelly, G. (2001). A satellite radiance-bias correction scheme for data assimilation. *Quarterly Journal of the Royal Meteorological Society*, *127*, 1453–1468.

Kunkee, D. B., Poe, G. A., Boucher, D. J., Swadley, S. D., Hong, Y., Wessel, J. E., et al. (2008). Design and evaluation of the first special sensor microwave imager/sounder. *IEEE Transactions on Geoscience and Remote Sensing*, *46*(4), 863–883.

Lu, Q., & Bell, W. (2014). Characterizing channel center frequencies in AMSU-A and MSU microwave sounding instruments. *Journal of Atmospheric and Oceanic Technology*, *31*(8), 1713–1732.

McNally, A. (2014). The impact of satellite data on global NWP. In *Proceedings of the ECMWF seminar on use of satellite observations in NWP*, pp. 8–12.

Prigent, C., Aires, F., & Rossow, W. B. (2006). Land surface microwave emissivities over the globe for a decade. *Bulletin of the American Meteorological Society*, *87*(11), 1573–1584.

Randall, D. (2012). *Atmosphere, clouds, and climate*. Princeton: Princeton University Press.

Saunders, R. W., Matricardi, M., & Brunel, P. (1999). An improved fast radiative transfer model for assimilation of satellite radiance observations. *Quarterly Journal of the Royal Meteorological Society*, *125*, 1407–1425.

Swadley, S. D., Poe, G. A., Bell, W., Hong, Y., Kunkee, D. B., McDermid, I. S., et al. (2008). Analysis and characterization of the SSMIS upper atmosphere sounding channel measurements. *IEEE Transactions on Geoscience and Remote Sensing*, *46*(4), 962–983.

Uspensky, S., Kramchaninova, E., Uspensky, A., Poli, P., English, S., and Lupu, C. (2015). An initial assessment of microwave imager/sounder MTVZA-GY data from Meteor-M N2 satellite. In *International TOVS study conference ITSC-XX: Lake Geneva, Wisconsin, USA, 28 October–3 November 2015*. IEEE.

Uspensky, A., Asmus, V., Kozlov, A., Kramchaninova, E., Streltsov, A., Chernyavsky, G., et al. (2017). Absolute calibration of the MTVZA-GY microwave radiometer atmospheric sounding channels. *Izvestiya Atmospheric and Oceanic Physics*, *53*(9), 1192–1204. (Original Russian text published in Issledovanie Zemli iz Kosmosa, 2016, N5, 57–70).

Weng, F., Zhao, L., Ferraro, R. R., Poe, G., Li, X., & Grody, N. C. (2003). Advanced microwave sounding unit cloud and precipitation algorithms. *Radio Science*, *38*(4), MAR33-1 - MAR33-13.

Weng, F., Zou, X., Wang, X., Yang, S., & Goldberg, M. (2012). Introduction to Suomi national polar-orbiting partnership advanced technology microwave sounder for numerical weather prediction and tropical cyclone applications. *Journal of Geophysical Research Atmospheres*, *117*, D19112.

Wessel, J., Farley, R. W., Fote, A., Hong, Y., Poe, G. A., Swadley, S. D., et al. (2008). Calibration and validation of DMSP SSMIS lower atmospheric sounding channels. *IEEE Transactions on Geoscience and Remote Sensing*, *46*(4), 946–961.

Zou, X., Lin, L., & Weng, F. (2014). Absolute calibration of ATMS upper level temperature sounding channels using GPS RO observations. *IEEE Transactions on Geoscience and Remote Sensing*, *52*(2), 1397–1406.

Zou, C.-Z., & Wang, W. (2011). Intersatellite calibration of AMSU-A observations for weather and climate applications. *Journal of Geophysical Research Atmospheres*, *116*, D23113.

(Received January 3, 2018, revised May 21, 2018, accepted May 31, 2018, Published online June 15, 2018)